A functional tool to explore the reliability of micro-earthquake focal mechanism solution for seismotectonic purposes

G.M. Adinolfi [1, 3, *], R. De Matteis [1], R. de Nardis [2, 3] and A. Zollo [4]

[1] Dipartimento di Scienze e Tecnologie, Università del Sannio ViaDe Sanctis, 82100 Benevento, Italy

[2] Dipartimento di Scienze Psicologiche, della Salute e del Territorio, Università di Chieti-Pescara "G. d'Annunzio", Via dei Vestini, 32, 66100, Chieti, Italy

[3] CRUST Centro inteRUniversitario per l'analisi SismoTettonica tridimensionale, Italy

[4] Dipartimento di Fisica, Università di Napoli "Federico II", Complesso Universitario di Monte S.Angelo, via Cinthia, 80124 Napoli, Italy

* Corresponding author: gmadinolfi@unisannio.it

ABSTRACT

Improving the knowledge of seismogenic faults requires the integration of geological, seismological, and geophysical information. Among several analyses, the definition of earthquake focal mechanisms plays an essential role in providing information about the geometry of individual faults and the stress regime acting in a region. Fault plane solutions can be retrieved by several techniques operating in specific magnitude ranges, both in the time and frequency domain and using different data.

For earthquakes of low magnitude, the limited number of available data and their uncertainties can compromise the stability of fault plane solutions. In this work, we propose a useful methodology to evaluate how well a seismic network, used to monitor natural and/or induced micro-seismicity, estimates focal mechanisms as a function of magnitude, location, and kinematics of seismic source and consequently their reliability in defining seismotectonic models. To study the consistency of focal mechanism solutions, we use a Bayesian approach that jointly inverts the P/S long-period spectral-level ratios and the P polarities to infer the fault-plane solutions. We applied this methodology, by computing synthetic data, to the local seismic network operating in the Campania-Lucania Apennines (Southern Italy) aimed to monitor the complex normal fault system activated during the Ms 6.9, 1980 earthquake. We demonstrate that the method we propose is effective and can be adapted for other case studies with a double purpose. It can be a valid tool to design or to test the performance of local seismic networks and more generally it can be used to assign an absolute uncertainty to focal mechanism solutions fundamental for seismotectonic studies.

INTRODUCTION

Fault plane solutions represent primary information that seismologists can retrieve to describe the earthquake source. The assessment of earthquake location, magnitude, and focal mechanism are the fundamental operations to characterize the earthquake source through the point source approximation. After the earthquake location, origin time, and source dimension are identified, the focal mechanism describes the basic geometry and kinematics of a point source in terms of strike, dip, and rake of the fault plane along which the earthquake occurred. So, the focal mechanism is the most important parameter that can be retrieved to recognize the geometry of the seismogenic faults and their style of faulting. Moreover, the seismicity and focal mechanisms of events, also of small magnitudes, are often used to constrain seismotectonic models, individual seismogenic sources, the regional strain, and stress fields. Consequently, an evaluation of their effective reliability becomes a fundamental issue in seismotectonic studies.

Nevertheless, focal mechanisms cannot be calculated and constrained every time an earthquake occurs. Although the calculation of focal mechanisms represents a routine analysis inside the seismological agencies, the solutions are calculated only for a specific range of magnitude, usually greater than 4. In fact, constraining the solution for earthquakes with small magnitude still represents a challenge, despite the advancement in the technological process and the use of increasingly performing seismic networks. This is due to several factors that we will analyse in detail. The techniques used to define the focal mechanism of large-moderate earthquakes are based on the inversion of the moment tensor, that corresponds to a stable and robust procedure, so much that it is the most common method for this type of analysis (Dreger, 2003; Delouis, 2014; Sokos and Zahradnik, 2013; Cesca et al., 2011). This technique requires accurate knowledge of the propagation medium in relation to the range of frequencies used for the modelling of the waveforms recorded during an earthquake. The smaller an earthquake, the higher the frequency range of the signal to be modelled, the more detailed the knowledge and scale of the Earth's interior must be. Several methods have been proposed to achieve a stable inversion of the moment tensor for earthquakes with a magnitude less than 3. Hybrid approach

of the amplitude and waveform moment tensor inversions, which utilizes the principal component analysis of seismograms (Vavrycuk et al., 2017) or moment tensor refinement techniques (Kwiatek et al. 2016; Bentz at al., 2018) facilitate a robust determination of the source type and its kinematics. In particular, the retrieved moment tensor is typically decomposed into volumetric and deviatoric components. Constraining the earthquake as double-couple source can erroneously affect the retrieved fault plane solutions, especially in the case of induced seismicity where the volumetric or non-double couple component must be considered (Kwiatek et al. 2016).

Other analytical techniques are based on the recognition of radiation pattern that describes the earthquake source. According to the position of seismic stations with respect to the source, seismic waves on seismograms show different amplitudes and polarities. These features are employed in a very simple way by several algorithms to constrain the geometry of the earthquake faulting through estimating the angular parameters strike, dip, and rake. The classical method (Raesenberg and Oppenheimer, 1985;) uses the P-wave polarities, but advanced ones use P- or S- wave amplitudes or amplitude ratios together with first motions (Snoke, 2003) to better constrain the focal mechanism of small earthquakes. In fact, the use of polarities alone is not convenient, especially if we consider micro-seismicity (M < 3). The reasons could be the limited number of available data, their uncertainties, and the difficulty of measuring the P-polarity with a sufficient degree of precision. For these reasons, different techniques using different types of measurements such as P-wave amplitudes (Julian and Foulger, 1996; Tarantino et al., 2019), P/S or S/P amplitude ratios measured in the time or the frequency domain (Kisslinger et al., 1981; Rau et al., 1996; Hardebeck and Shearer, 2003; De Matteis et al., 2016), or S-wave polarizations (Zollo and Bernard, 1991) have been developed. The joint inversion of polarities and amplitude ratios led to more stable and robust solutions, allowing to account for geological site effects and to decrease in first approximation the effects produced by the geometric and anelastic attenuations.

Two kinds of errors generally influence the goodness of the solution and retrieved model (Michele et al., 2016): the perturbation errors that are related to how the uncertainty on data affects the model,

93 and the resolution errors that are referred to the capability to retrieve a correct model, given a dataset
94 as input or how accurate could be the model that we can recover, even if error-free data are used. The
95 sum of perturbation and resolution errors corresponds to the final errors on the model obtained by
96 solving an inverse problem, as the solution of focal mechanism. In particular, the resolution errors
97 depend on the available data, and so on the initial condition of the inverse problem. In the case of focal
98 mechanism, the number of seismic stations, as well as the seismic network geometry, and the velocity
99 structure of the crust influence the resolution and the reliability of the retrieved model.

100 How will the geometry of a seismic network determine the accuracy of focal mechanism solutions? The
101 answer to this question is not simple and requires a deep knowledge of the geophysical and geological
102 characteristics of the region, often unrealistic. Moreover, the theoretical relationships that predict the
103 focal mechanism solutions for an earthquake scenario could be very complicated if several factors, such
104 as network configuration, noise level, source magnitude, or source kinematics are taken into account.
105 We want to underline that a network configuration may be optimal for earthquake locations, but not for
106 retrieving fault plane solutions (Hardt and Scherbaum, 1994). In fact, a given geometry may resolve
107 some fault kinematics better than others.

108 A seismic network layout is strictly associated with the goals of the network and the available funds;
109 according to these features, a network operator decides how many stations are required and where
110 they should be located (Havskov et al.; 2011). So, the number of seismic stations, the size, and geometry
111 of the network are defined after a preliminary phase based on the evaluation of the specific
112 seismological target (Trnkoczy et al., 2009; Hardt and Scherbaum 1994; Steinberg et al. 1995; Bartal
113 et al. 2000). In the case of small earthquakes, the available recordings come from only a portion of the
114 total network, while the distant stations show a seismic signal buried in the noise. In order to detect
115 and locate low-magnitude earthquakes, we must increase the number of seismic stations for area units
116 by building a dense seismic network.

117 In this study, we propose a useful tool to evaluate both 1) the reliability of focal mechanism solutions
118 inferred by the inversion of different seismological data and 2) the performance of the seismic network

119   to assess focal mechanism solutions and their errors. We evaluate the network capability to solve focal

120   mechanisms as a function of magnitude, location, and kinematics of seismic source. We consider three

121   synthetic data set: P-wave polarities, P- S-wave amplitude spectral ratios and polarities and amplitude

122   ratios together. Moreover, different levels of noise are considered in order to simulate more realistic

123   conditions.

124   We selected as target the Irpinia Seismic Network (ISNet), a local seismic network that monitors the

125   Irpinia complex normal fault system (Southern Italy), activated during the Ms 6.9 earthquake of 23rd

126   November 1980. Evaluating the specific performance of an existing network for a seismological goal is

127   critical and can be used to decide how to improve its layout.

128

METHODOLOGY

130   With the main aim to define the reliability of focal mechanisms retrieved by specific seismic networks,

131   we propose a methodology based on an empirical approach that consists of different steps.

132   *Configuration and Parameter Tuning (Step 1).* In a preliminary phase, we select for each earthquake

133   simulation the: a) fault plane solution to test, b) seismic observables to be computed (i.e. P-wave

134   polarities or P- S-wave amplitude spectral ratios), c) magnitude, d) the earthquake epicentre and depth;

135   e) the network geometry; f) the noise level. The fault plane solution to test can be derived from

136   instrumental seismicity as one of the strongest earthquakes occurred in the area or a median solution

137   of the available ones or simply a fault plane solution representative of the regional seismotectonic.

138   Once the network geometry and the hypocentre of the earthquake are defined, the seismic stations

139   (number and type) for which the synthetic data are computed must be selected. The number of seismic

140   stations that record an event depends on earthquake magnitude, source-stations distance, crustal

141   medium properties, and the level of noise. We use an empirical approach, based on the statistical

142   analysis of the local seismicity catalog, that allows us to define, for each magnitude range, a maximum

143 (threshold) epicentral distance for which only the seismic stations within this distance are considered

144 (See data analysis).

145 *Synthetic Data Computation (Step 2).* Using a crustal velocity model and the source-receiver relative

146 position, the synthetic data are computed for the theoretical fault plane solution. The seismic

147 observables that can be reproduced are a) P-wave polarities, b) P/S spectral amplitude ratios, and c)

148 polarities and amplitude ratios together. For the P/S spectral level ratios, the Gaussian noise level is

149 added.

150 *Focal Mechansim Inversion (Step 3).* We estimated focal mechanism using BISTROP code (De Matteis

151 et al., 2016) that jointly inverts the ratio between the P- and S-wave long-period spectral levels and

152 the P-wave polarities according to a Bayesian approach. BISTROP has the advantage to use different

153 observables for the determination of fault plane solutions, such as the P/S long-period spectral level

154 ratios or P-wave polarities, individually or together. The benefits of the use of spectral level ratios are

155 multiples: 1) they can be measured for a broad range of magnitudes (also for M < 3; De Matteis et al.,

156 2016); 2) they can be calculated by automatic procedures without visual inspection; 3) their estimates

157 do not require to identify the first arrival time accurately, but only a time window of signal containing

158 P- or S-phase is mandatory and 4) the spectral amplitude ratios, they can generally be used without

159 the exact knowledge of the geological soil conditions (site effects) and geometric/anelastic attenuation.

160 Moreover, the joint inversion of amplitude spectral ratios and polarities led to constraining fault plane

161 solutions reducing the error associated with the estimates of retrieved parameters. BISTROP solves an

162 inverse problem through a probabilistic formulation leading to a complete representation of uncertainty

163 and correlation of the inferred parameters.

164 For a double-couple seismic source, the radiation pattern depends on fault kinematics and relative

165 source-station position. In fact, it can be represented as a function of 1) strike, dip and rake angles (φ,

166 δ, λ) and 2) take-off and azimuth angles (i_h, φ_r). We can define the ratio between P- and S-wave

167 radiation pattern coefficients as:

$$\frac{\mathcal{R}^P\left(\phi, \delta, \lambda, i_h, \phi_R\right)}{\mathcal{R}^S\left(\phi, \delta, \lambda, i_h, \phi_R\right)} = \left(\frac{\alpha_s^2 \alpha_r}{\beta_s^2 \beta_r}\right) \frac{\Omega_0^P}{\Omega_0^S} \qquad (1)$$

where Ω_0^P and Ω_0^S are the long-period spectral level of the P- and S-waves, respectively, and α_s, α_r, β_s, β_r, are the P- and S-wave velocities at the source and at the receiver, respectively. Thus, using the displacement spectra, assuming a given source and attenuation model (Boatwright, 1980), we can derive from the signal recorded by a seismic station the ratio of radiation pattern coefficients for P- and S-phases, as well as α, β, i_h, φ_r are known from the earthquake location and the velocity model used. So, from a theoretical point of view, the spectral amplitude ratios measured at several seismic stations can be used to retrieve the ratio of radiation pattern coefficients $\mathcal{R}_{\theta\varphi}^P/\mathcal{R}_{\theta\varphi}^S$ as a function of the source-receiver azimuth and take-off angles.

BISTROP jointly inverts the spectral amplitude ratios with the observed P-wave polarities to infer the parameters φ, δ, λ of the focal mechanism in a Bayesian framework. A posterior probability density function (PDF), for the vector of model parameter $\boldsymbol{m}$ (φ, δ, λ) and the vector of observed data $\boldsymbol{d}$, is defined as:

$$q(\boldsymbol{m}|\boldsymbol{d}) = \frac{f(\boldsymbol{d}|\boldsymbol{m})p(\boldsymbol{m})}{\int_M f(\boldsymbol{d}|\boldsymbol{m}')p(\boldsymbol{m}')\,d\boldsymbol{m}'} \qquad (2)$$

where $f(\mathbf{d}|\mathbf{m})$ is the conditional probability function that represents the PDF given the data $\mathbf{d}$ and for parameter vector $\boldsymbol{m}$ in the model parameter space $\boldsymbol{M}$, and $p(\boldsymbol{m})$ is the a priori PDF. If P-wave polarities and P/S spectral level ratios are independent datasets, the conditional probability function may be written as:

$$f(\mathbf{d}|\mathbf{m}) = f(\boldsymbol{d}^L|\mathbf{m})f(\boldsymbol{d}^P|\mathbf{m}). \qquad (3)$$

in which the pdf of the data vector d^L of N^L measurements of spectral ratios is multiplied for the pdf of data vector d^P of N^P measurements of P-wave polarities given the model m.

Assuming that the observables have the same finite variance, for the N^L observations of spectral level ratios the conditional probability function may be defined as:

$$f(d^L|m) = \frac{1}{(\sqrt{2\pi}\sigma\ )^{N_L}} exp\left(-\frac{\sum_{i=1}^{N_L}\{d_i - [G(m)]_i\}^2}{2\sigma^2}\right) \tag{4}$$

Where $G(m)$ represents a functional relationship between model and data and corresponds to Equation 1 and σ represents the uncertainty on the spectral measure.

For the N^P observations of P-wave polarities, the conditional probability function is (Brillinger et al., 1980):

$$f(d^P|m) = \prod_{i=1}^{N_P}\frac{1}{2}[1 + \psi(\mathcal{R}_i^P,\gamma_i,\rho_0)Y_i sign(\mathcal{R}_i^P)] \tag{5}$$

in which:

.

$$\psi(\mathcal{R}_i^P,\gamma_i,\rho_0) = (1 - 2\gamma_i)\,\text{erf}(|\rho_0\mathcal{R}_i^P(m)|) \tag{6}$$

The quantity reported in square brackets in Equation 5 represents the probability that the observed i_{th} polarity γ_i is consistent with the theoretical one computed from the model m, whose theoretical P-wave amplitude is $\mathcal{R}_i^P$ and $sign(\mathcal{R}_i^P)$ is its polarity at i_{th} station for a given fault plane solution. The parameters ρ_s and γ_0 , referring to the errors in ray tracing due to velocity model ambiguity and to the

210 uncertainty on polarity reading, regulating the shape of the PDF. For more details about the

211 mathematical formulation, see De Matteis et al. (2016).

212 *Evaluation of the Results (Step 4).* Once the best solution is estimated, the focal mechanism

213 uncertainties and its misfit, respect to the theoretical solution as Kagan angle, are computed. The focal

214 mechanism parameter (strike, dip and rake) misfit and their uncertainties are also calculated.

215

216 **IRPINIA SEISMIC NETWORK**

217 As testing case of our methodology, we choose the area of the M 6.9, 1980 Irpinia earthquake

218 (Southern Italy). Since 2005, ISNet, a local, dense seismic network monitors the seismicity along the

219 Campania-Lucania Apennines covering an area of about 100×70 km^2 (Figure 1; Weber et al., 2007).

220 The seismic stations are deployed within an elliptic area whose major axis, parallel to the Apennine

221 chain, has a NW-SE trend with an average inter-stations distance of 15 km that reaches 10 km in the

222 inner central zone. Each seismic station ensures a high dynamic range and it is equipped with a strong-

223 motion accelerometer, Guralp CMG-5T or Kinemetrics Episensor, and a short period three-component

224 seismometer, Geotech S13-J with a natural period of 1 sec. In 6 cases, broadband seismometers are

225 installed such as the Nanometrics Trillium with a flat response in the range 0.025–50 Hz. ISNet is

226 operating by INFO (Irpinia Near Fault Observatory) and it provides real-time data at local control centres

227 for earthquake early warning systems or real-time seismic monitoring (Satriano et al., 2011). Seismic

228 events are automatically identified and located from continuous recordings by automatic Earth-worm

229 Binder and data are then manually revised by operators (Festa et al., 2020).

230 The 1980, M 6.9, Irpinia earthquake was one of the most destructive, instrumental earthquakes of the

231 Southern Apennines, causing about 3000 fatalities and severe damages in the Campania and Basilicata

232 regions. It activated a NW-SE trending normal fault system with a complex rupture process involving

233 multiple fault segments according to (at least) three different nucleation episodes delayed each other

234 of 20 s (Bernard and Zollo, 1989; Pantosti and Valensise; 1993; Amoruso et al.; 2005). No large

235 earthquakes occurred in the Irpinia region since 1980. A Mw 4.9 earthquake took place in 1996

236 originating a seismic sequence inside the epicentral area of the 1980 earthquake (Figure 1; Cocco et

237 al., 1999). Recent instrumental seismicity occurs mainly in the first 15 km of the crust showing fault

238 plane solutions with normal and normal-strike slip kinematics, indicating a dominant SW-NE extensional

239 regime (Pasquale et al., 2009; De Matteis et al., 2012; Bello et al., 2021). Low-magnitude seismicity

240 ($M_L < 3.6$) is spread into a large volume related to the activity of major fault segments of the 1980

241 Irpinia earthquake (Figure 1; Adinolfi et al., 2019; Adinolfi et al., 2020). Seismic sequences or swarms

242 often occurred in the area, extremely clustered in time (from several hours to a few days) and space

243 and seem to be controlled by high pore fluid pressure of saturated Apulian carbonates bounded by

244 normal seismogenic faults (Stabile et al., 2012; Amoroso et al, 2014).

245

DATA ANALYSIS

247 We applied the method we proposed and evaluated the capability of the ISNet local network to resolve

248 fault plane solutions using different observables as input data: a) P-wave polarities, b) P/S spectral

249 amplitude ratios and c) polarities and amplitude ratios together. the analysis is carried out by evaluating

250 the effect of 1) earthquake magnitude, 2) epicentral location, 3) earthquake depth, 4) signal-to-noise

251 ratio, and 5) fault kinematics on retrieved focal solutions as previously described.

252 *Step 1*. In order to selectfocal mechanisms (FMs) to be used for our resolution study (Figure 2a), we

253 carried out statistical analysis to define the most frequent fault plane solutions of instrumental

254 seismicity. We classified, according to the plunge of P- and T-axes, the fault plane solutions reported

255 in De Matteis et al. (2012) choosing only the FMs occurring within the Irpinia area since 2005 to 2011.

256 As shown in Figure 2b, splitting the range of the data into equal-sized bins, we selected the focal

257 mechanism corresponding to the median value of the most populated class. We report it in Figure 2a

258 as FM2. This corresponds to a normal-strike-slip fault plane solution with strike, dip, and rake equal to

259 292°, 53°, and -133°, respectively. Then, we decided to test the focal mechanism solution of the1980

Irpinia earthquake, a pure normal fault (strike, dip, rake: 317°, 59°, -85°; Westaway and Jackson, 1987; Fig. 2a) here and after FM1. This solution is very similar to the focal mechanism corresponding to: 1) the regional stress field (see Supplementary Material); 2) the M_L 2.9, Laviano earthquake, one of the most energetic earthquakes of the last years (Stabile et al.; 2012), and 3) those of the 2nd, 3rd, 4th most populated bins. Finally, we selected the solution corresponding to the 5th bin reported as FM3 in Figure 2a. This focal mechanism is quite different from the others due to a predominant component along the fault strike (strike, dip, rake: 274°, 71°, -128°)

Step 2. For each of the three selected fault plane kinematics, we calculated synthetic data (P-wave polarities or P- and S-wave spectral amplitudes) at seismic stations varying the earthquake location and by using a local velocity model (Matrullo et al., 2013). We discretize the study area with a square grid (100 X 100 km^2), centred on the barycentre of ISNet, with 441 nodes and a sampling step of 5 km. Each node corresponds to a possible earthquake epicentre (Figure 3).

For each grid node and according to the earthquake magnitude to be tested, we have to select the ISNet stations for simulations. The number of seismic stations that record an event depends on earthquake magnitude, source-stations distance, crustal medium properties, and the noise level. Theoretical relationships that link the seismic source to the signal recorded at every single station are quite complicated (Kwiatek et al., 2016; 2020) and are based on the accurate knowledge of crustal volumes in which the seismic waves propagated, such as the three-dimensional wave velocity structure, anelastic attenuation or/and site conditions of a single receiver. To overcome this limitation, we used an empirical approach to define the number and the distance of the seismic stations that record a seismic signal as a function of magnitude, once its epicentral location (grid node) and depth are fixed. Using the bulletin data retrieved by INFO at ISNet during the last two years (January 2019-March 2021; http://isnet-bulletin.fisica.unina.it/cgi-bin/isnet-events/isnet.cgi), we selected two earthquake catalog datasets with depths equal to 5 (+- 2) km and 10 (+- 2) km, respectively, and local magnitude ranging between 1.0 and 2.5. These choices are motivated by the characteristics of the Irpinia micro-seismicity recorded by ISNet. Then, we divided each dataset into bins of 0.5 magnitudes and for each bin, we

286   retrieved the median number of P-wave polarity readings and the median epicentral distance of the

287   farthest station that recorded the earthquake (Table 1). The bulletin data are manually revised by

288   operators, and we selected only seismic records that provide P- and/or S- wave arrival times. The

289   median value of the distance of the farthest station is then used to select the seismic stations for which

290   synthetic data are calculated. Therefore, for each earthquake simulation of specific magnitude and

291   depth, only the seismic stations with a distance, from the grid node under examination (epicentre), equal

292   or lower than the maximum distance, reported in Table 1, are considered. We run simulations only for

293   earthquakes recorded at least by 6 seismic stations. The synthetic P-wave polarities are simulated only

294   at a number of stations corresponding to the median value previously defined. (Table 1). We pointed

295   out that the number of P-wave polarities empirically assigned is related to the available earthquake

296   catalogue data of the Irpinia region where the seismicity can occur in different portions of the area

297   covered by the network, not always with optimal azimuthal coverage.

298   Additionally, we simulated the uncertainty on the measure of spectral level ratios or the effect of seismic

299   noise adding a zero mean, Gaussian noise to the synthetic data with a standard deviation equal to two

300   different percentage levels, as 5% and 30%. With this configuration, we simulated:

301   • Three datasets of seismic observables: P-wave polarities (D1), P/S spectral level ratios (D2) and

302   polarities and P/S spectral level ratios together (D3)

303   • Two hypocentre depths: 5 km and 10 km

304   • Three magnitude bins: M_L 1.0 -1.5 (M1), M_L 1.5 - 2.0 (M2) and M_L 2.0 - 2.5 (M3)

305   • Three focal mechanism solutions: FM1 (317°, 59°, -85°), FM2 (292°, 53°, -133°) and FM3

306   (274°, 71°, -128°)

307   Two level of Gaussian noise: 5% and 30%. When D2 is simulated, in order to solve the verse ambiguity

308   of the slip vector, a P-wave polarity is added to the earthquake data to be inverted for the focal

309   mechanism.

310   *Step 3*. For each earthquake simulation the focal mechanism was estimated by inverting the synthetic

311   data with BISTROP (De Matteis et al.; 2016).

312 *Step 4.* In order to analyse the results, we defined five kinds of map to study how the focal mechanism

313 (FM) resolution and error spatially change in the area where ISNet is installed (Table 2):

314

315 • Kagan angle misfit map (KAM)

316 • Map of the focal mechanism parameter misfit (FMM)

317 • Strike, Dip and Rake error map (FME)

318 • Kagan angle average map (KAA)

319 • Kagan angle standard deviation map (KAS)

320

321 The Kagan Angle (KA) measures the difference between the orientations of two seismic moment tensors

322 or two double couples. It is the smallest angle needed to rotate the principal axes of one moment tensor

323 to the corresponding principal axes of the other (Kagan et al.; 1991; Tape and Tape; 2012). The smaller

324 the KA between two focal mechanisms, more similar they are. In KAM map, for each node the value of

325 KA between the theoretical and retrieved solution is reported, while in FMM map, the absolute value of

326 the misfit between the strike, dip, and rake angles of the retrieved and theoretical solution is indicated.

327 FME is defined as the error map of strike, dip, and rake in which the uncertainties (standard deviations)

328 are calculated considering all the solutions with probability larger than the 90% (S90) of the maximum

329 probability, corresponding to the best solution retrieved. Additionally, these solutions are used to study

330 how constrained is the FM solution. The KA is calculated between each FM of S90 solutions and the

331 retrieved best solution. The mean and the standard deviation of the resulting KA distribution are plotted

332 in KAA and KAS maps, respectively. The smaller KA mean and std, the more constrained is the obtained

333 fault plane solution (Table 2).

334

335 **DISCUSSION**

336 We consider the FM1, i.e. the focal mechanism of the 1980 Irpinia earthquake located at 10 km depth,

337 first. Looking at Figures 4 and 5, we see the effect of using the three different datasets. Considering

338 D1, we can calculate the FM only for earthquakes with magnitude 2.0-2.5 for which at least 6 polarities

339 are available. As shown by KAM map in Figure 4a, the retrieved solutions are characterized by high KA

340 (> 50°) with limited areas or single nodes with values in the range 40°-50°. Therefore, D1 is not

341 sufficient to retrieve with acceptable accuracy the FMs for earthquakes with magnitude 2.0-2.5. The

342 same result is obtained for FM2 and FM3 (Figure 4b-c). Comparing the results of the simulations using

343 D2 and D3 (Figure 5), the accuracy of the retrieved solution is improved when P-wave polarities data

344 are added to spectral level ratios. The areas in KAM map with high value of KA (KA $\geq$ 18°; red or green

345 areas) disappear or are strongly reduced. Nevertheless, we want to underline that, even with D2 dataset,

346 exception some small areas, the FMs are well retrieved for all magnitudes with the KA misfit mostly

347 lesser than 10°. The spatial resolution of the network is strongly influenced by the earthquake

348 magnitude. In fact, for both M1 and M2, there are nodes (white areas where we assume the KA = -1 as

349 an indeterminate value) for which the FMs cannot be calculated because a minimum number of stations

350 (at least 6) are not available (Table 1). At the same time, the areas better resolved correspond to the

351 region inside the network, although with D2 and D3 acceptable solutions are calculated for M1 and

352 M2 earthquakes also outside the network, (Figure 5).

353 Looking at Figure 6, using the D3 dataset, we observe that, among the FM parameters, the dip angle

354 is the best resolved compared with strike and rake angles. Considering M2 and M3 focal mechanisms,

355 the misfit of dip is very low (< 8°), followed, in ascending order, by rake and strike that show higher

356 values (10° < misfit < 22°). For M1 (Figure 6a-d-g), rake and strike misfits are larger than 50°, with

357 rake worse resolved than strike. The unresolved areas correspond to the regions outside the seismic

358 network.

359 The KAA and KAS maps (Figures 7 and 8) show how the network constrains the fault plane solution as

360 a function of the epicentral location. Moreover, Figures 7d-e-f and 8d-e-f indicate that the areas with

361 KA mean and std greater than 30° and 20°, respectively, are reduced when P-wave polarities and

362 spectral level ratios data are used. On contrary, only for M1 focal mechanisms, there is no improvement

363 because the number of P-wave polarities is the same for both D2 and D3 datasets (Table 1). The worst

364 constrained regions correspond to a belt surrounding the seismic network, with KA mean < 30° and

KA std < 20° for M2 and M3 solutions. For M1, areas with high uncertainty remain outside and inside the network, specifically in the central and eastern sectors.

Looking at the uncertainties of FM parameters, obtained by using the D3 dataset, Figure 9 shows that the dip is the better-constrained parameter with an error < 10°, also for M1 solutions. The rake angle shows an uncertainty lesser than 20° for M2 and M3, while it overcomes 50° for M1. The strike angle reveals the highest uncertainty, with values greater than 50° in the eastern and southern sectors of the map for all analysed magnitudes (M1, M2, and M3). Accuracy improves moving from M1 to M3 earthquakes.

As shown in Figure 10, the accuracy of fault plane solutions, in terms of KA misfit calculated by using the D3 dataset, is similar for FM1, FM2, and FM3, mostly with values lesser than 8° for all the magnitudes M1, M2, and M3. FM2 and FM3 show a slightly higher precision than FM1 in the area inside the seismic network (see FMM, FME, KAA, and KAS maps for FM2 and FM3 in Supplementary Material). In the regions outside the network, where the azimuthal gap increases, the FMs better constrained in descending order are: FM3, FM2, and FM1. This effect should be due to the geometric relationship between the spatial distribution of the seismic stations and the orientation of the principal axes (P, T, B) that characterize the FMs.

Considering the effect of hypocentre depth, the results achieved for earthquakes at 5 km depth, by using the D3 dataset, are overall unchanged (Figure 11). We note that the fault plane solutions are slightly worse resolved due to a smaller number of P-wave polarities available for M2 and M3. The KA misfit mainly is lesser than 10°, even though the number and the dimension of areas with misfits> 20° are greater than those obtained considering earthquakes at 10 km depth. Moreover, the dip angle shows a misfit lower than strike and rake angles for M1, M2, and M3; the accuracy of the retrieved FMs parameters is mainly lesser than 8°, as shown in Figure 11.

Previous analyses are carried out considering by using data affected by 5% Gaussian error. In the last test, we simulated synthetic data adding a 30% Gaussian error. As illustrated in Figure 12, FM solutions show an overall larger misfit, in particular, the KA inside the seismic network is less than 20°. The area best resolved (KA < 8°) is considerably reduced to a small central portion of the network. This result

indicates that the accuracy of the spectral level ratio estimates is crucial: noisy waveforms with a low signal-to-noise ratio can critically affect the result of the focal mechanism inversion. So, seismic noise as well as the number of available stations, variable due to the operational condition, strongly influence the capability of the seismic network to retrieve fault plane solution. Using the results of our simulations, we classified the focal mechanism provided by De Matteis et al. (2016) according to a quality code based on the resolution of fault kinematics (Table 3). In fact, we assigned to focal mechanisms of Irpinia instrumental seismicity a quality A, B and C for the solutions that fall into the bins relative to FM3, FM2 and FM1 kinematics, respectively. The quality A, B and C correspond to the average value of KA misfit (FM3=2.4°, FM2=3.1°, FM1=4.5°) calculated for M1, M2 and M3 magnitudes using D3 dataset and considering earthquakes at 10 km depth with 5% Gaussian errors.

As last analysis, we carried out a test in a more general framework, without a fixed network configuration. We explored the reliability of focal mechanism estimation as a function of the uniformity focal sphere coverage defined by the number of recording seismic stations and azimuthal gap. We simulated 10400 earthquakes fixing the fault plane solution and varying: 1) the number of seismic stations (6-30), 2) take-off angle and 3) azimuth of each single station. For each possible number of seismic stations, we run about 400 simulations, and we randomly sampled the focal sphere varying the azimuth and take-off of the stations and, so, changing the geometrical configuration of our virtual network of each simulation. We computed the KA between the theoretical and retrieved focal mechanism (best) solutions, using only P-polarities, for each simulation. We show the results in the Figures 13 and S7, as 3-D histograms and 3-D scatter plot, respectively. In the Figures 13a, as expected, we note that, as the number of stations increases, the KA and its range of variation decrease. If the number of stations is less than nine, only few solutions have KA<40°. Figure 13b shows that the most value of KA less than 30° are obtained for azimuthal gap less than about 80°. Moreover, these evidences are shown in the Figure S7, where the relation among the KA, azimuthal gap and number of stations is clear by the three-dimensional spatial point patterns as well by the projections of the data on the three coordinate planes.

CONCLUSIONS

We studied the focal mechanism reliability retrieved by the inversion of data recorded by ISNet, a local dense seismic network that monitors the Irpinia Fault System in Southern Italy. Three different datasets of seismological observables are used as input data for focal mechanism determination: a) P-wave polarities, b) P/S long-period spectral amplitude ratios and c) joint polarities and amplitude ratios. Starting from empirical observations, we computed synthetic data for a regular grid of epicentre locations at two depths (5 and 10 km), for earthquake magnitude in the range 1.0-2.5 and for three focal mechanism solutions. Two different levels of Gaussian error (5% and 30%) are added to the data.

Main conclusions can be summarized as follows.

- The joint inversion of P-wave polarities and P/S spectral amplitude ratios allows retrieving accurate FM (KA misfit < 8°) also for earthquakes with magnitude ranging between 1.0 and 2.5, at depth of 5 and 10 km. Due to the low-energy magnitude, the number of P-wave polarities is not adequate to constrain fault plane solutions.

- The spatial resolution analysis of ISNet shows that the most accurate FM solutions are obtained for earthquakes located inside the network with strike, dip and rake misfit < 8°. Nevertheless, outside the network or at its borders, acceptable solutions can be calculated even if the azimuthal coverage is not adequate (especially for M2 and M3 events). This peculiarity is due to the geometrical relationship between the recording seismic stations and the orientation of principal axes (P, T, B).

- The geometry of the network allows to well resolve fault plane solutions varying between normal and normal-strike focal mechanism with mainly strike, dip and rake misfit lesser than 10° for magnitude range 1.5-2.5. The network resolves a slightly better normal-strike fault plane solution than a pure normal focal mechanism.

- Among the FM parameters, the dip angle shows the lowest uncertainty. Strike and rake angles reveal higher errors especially for M 1-1.5 earthquakes in the region outside the seismic network.

- Dataset affected by 30% Gaussian error provide a worsening in the accuracy of the retrieved FMs. Although the high error level, the area of well resolved fault plane solutions (KA misfit < 20°) persists in the central part of the network, especially for M2 and M3.

The methodology described in this work can be a valid tool to design or to test the performance of local seismic networks, aimed at monitoring natural or induced seismicity. Moreover, given a network configuration, it can be used to evaluate the reliability of FMs or to classify the retrieved fault plane solutions that represent a fundamental information in seismotectonic studies. Although it is a theoretical study, many earthquake scenarios with several magnitude, locations and noise conditions can be simulated to mimic the real seismicity.

REFERENCES

Adinolfi, G. M., Cesca, S., Picozzi, M., Heimann, S., & Zollo, A. (2019). Detection of weak seismic sequences based on arrival time coherence and empiric network detectability: an application at a near fault observatory. *Geophysical Journal International*, *218*(3), 2054-2065.

Adinolfi, G. M., Picozzi, M., Cesca, S., Heimann, S., & Zollo, A. (2020). An application of coherence-based method for earthquake detection and microseismic monitoring (Irpinia fault system, Southern Italy). *Journal of Seismology*, *24*, 979-989.

Amoroso, O., Ascione, A., Mazzoli, S., Virieux, J., & Zollo, A. (2014). Seismic imaging of a fluid storage in the actively extending Apennine mountain belt, southern Italy. *Geophysical Research Letters*, *41*(11), 3802-3809.

Amoruso, A., Crescentini, L., & Scarpa, R. (2005). Faulting geometry for the complex 1980 Campania-Lucania earthquake from levelling data. *Geophysical Journal International*, *162*(1), 156-168.

Bartal, Y., Somer, Z., Leonard, G., Steinberg, D. M., & Horin, Y. B. (2000). Optimal seismic networks in Israel in the context of the Comprehensive Test Ban Treaty. *Bulletin of the seismological society of America*, *90*(1), 151-165.

Bello, S., De Nardis, R., Scarpa, R., Brozzetti, F., Cirillo, D., Ferrarini, F., ... & Lavecchia, G. (2021). Fault Pattern and Seismotectonic Style of the Campania–Lucania 1980 Earthquake (M w 6.9, Southern Italy): New Multidisciplinary Constraints. Front. *Earth Sci*, *8*, 608063.

Ben-Menahem, A., and S. J. Singh (1981). Seismic Waves and Sources, 1108 p, Springer-Verlag, New York.

Bentz, Stephan, P. Martínez-Garzón, G. Kwiatek, M. Bohnhoff, and J. Renner (2018). Sensitivity of Full Moment Tensors to Data Preprocessing and Inversion Parameters: A Case Study from the Salton Sea Geothermal Field. Bull. Seismol. Soc. Am. 108, 588–603, doi 10.1785/0120170203

Bernard, P., & Zollo, A. (1989). The Irpinia (Italy) 1980 earthquake: detailed analysis of a complex normal faulting. *Journal of Geophysical Research: Solid Earth*, *94*(B2), 1631-1647.

Boatwright, J. (1980). A spectral theory for circular seismic sources; simple estimates of source dimension, dynamic stress drop, and radiated seismic energy, *Bull. Seismol. Soc. Am.*, **70** (7), 1–27.

Brillinger, D. R., A. Udías, and B. A. Bolt (1980). A probability model for regional focal mechanism solutions, *Bull. Seism. Soc. Am.* **70**, 149- 170.

Cesca, S., Heimann, S., Stammler, K., & Dahm, T. (2010). Automated procedure for point and kinematic source inversion at regional distances. *Journal of Geophysical Research: Solid Earth*, *115*(B6).

Cocco, M., Chiarabba, C., Di Bona, M., Selvaggi, G., Margheriti, L., Frepoli, A., ... & Campillo, M. (1999). The April 1996 Irpinia seismic sequence: evidence for fault interaction. *Journal of Seismology*, *3*(1), 105-117.

Delouis, B. (2014). FMNEAR: Determination of focal mechanism and first estimate of rupture directivity using near-source records and a linear distribution of point sources. *Bulletin of the Seismological Society of America*, *104*(3), 1479-1500.

De Matteis, R., Matrullo, E., Rivera, L., Stabile, T. A., Pasquale, G., & Zollo, A. (2012). Fault delineation and regional stress direction from the analysis of background microseismicity in the southern Apennines, Italy. *Bulletin of the Seismological Society of America*, *102*(4), 1899-1907.

De Matteis, R., Convertito, V., & Zollo, A. (2016). BISTROP: Bayesian inversion of spectral-level ratios and P-wave polarities for focal mechanism determination. *Seismological Research Letters*, *87*(4), 944-954.

Dreger, D. S., Lee, W. H. K., Kanamori, H., Jennings, P. C., & Kisslinger, C. (2003). Time-domain moment tensor INVerse codel (TDMT-INVC) release 1.1. *International Handbook of Earthquake and Engineering Seismology, WHK Lee, H. Kanamori, PC Jennings, and C. Kisslinger (Editors), Vol. B*, 1627.

Festa, G., Adinolfi, G. M., Caruso, A., Colombelli, S., De Landro, G., Elia, L., ... & Zollo, A. (2021). Insights into Mechanical Properties of the 1980 Irpinia Fault System from the Analysis of a Seismic Sequence. *Geosciences*, *11*(1), 28.

Hardebeck, J., and M. Shearer (2003). Using S/P Amplitude Ratios to Constrain the Focal Mechanisms of Small Earthquakes, *Bull. Seism. Soc. Am.* **93**, 6, pp. 2434–2444, December 2003.

Hardt, M., & Scherbaum, F. (1994). The design of optimum networks for aftershock recordings. *Geophysical Journal International*, *117*(3), 716-726.

Havskov, J., Ottemöller, L., Trnkoczy, A., Bormann, P. (2012): Seismic Networks. - In: Bormann, P. (Ed.), *New Manual of Seismological Observatory Practice 2 (NMSOP-2)*, Potsdam : Deutsches GeoForschungsZentrum GFZ, 1-65.

Julian, B. R., and G. R. Foulger (1996). Earthquake mechanisms from linear-programming inversion of seismic-wave amplitude ratios, *Bull. Seism. Soc. Am.* **86** (4), 972-980.

Kagan, Y. Y. (1991). 3-D rotation of double-couple earthquake sources. *Geophysical Journal International*, *106*(3), 709-716.

Kisslinger, C., J. R. Bowman, and K. Koch (1981). Procedures for computing focal mechanisms from local (SV/P) z data, *Bull. Seism. Soc. Am.* **71** (6), 1719-1729.

Kwiatek, G., P. Martínez-Garzón, and M. Bohnhoff (2016). HybridMT: A MATLAB Software Package for Seismic Moment Tensor Inversion and Refinement. Seismol. Res. Lett.

Kwiatek, G. and Y. Ben-Zion (2016). Theoretical limits on detection and analysis of small earthquakes. Journal of Geophysical Research-Solid Earth 121, doi 10.1002/2016JB012908

Kwiatek, G. and Y. Ben-Zion (2020). Detection Limits and Near-Field Ground Motions of Fast and Slow Earthquakes. Journal of Geophysical Research: Solid Earth 125, e2019JB018935, doi 10.1029/2019JB018935

Matrullo E., R. De Matteis, C. Satriano, O. Amoroso, and A. Zollo (2013). An improved 1D seismic velocity model for seismological studies in the Campania-Lucania region (Southern Italy), *Geophys. J. Int.* **195**, Issue 1, pp.460-473, doi: 10.1093/gji/ggt224.

Michele, M., S. Custódio, and A. Emolo (2014). Moment tensor resolution: case study of the Irpinia Seismic Network, Southern Italy, *Bull. Seismol. Soc. Am.* **104**, 1348-1357, doi: 10.1785/0120130177.

Pantosti, D., & Valensise, G. (1990). Faulting mechanism and complexity of the November 23, 1980, Campania-Lucania earthquake, inferred from surface observations. *Journal of Geophysical Research: Solid Earth*, *95*(B10), 15319-15341.

Pasquale, G., De Matteis, R., Romeo, A., & Maresca, R. (2009). Earthquake focal mechanisms and stress inversion in the Irpinia Region (southern Italy). *Journal of seismology*, *13*(1), 107-124.

Reasenberg, P., & Oppenheimer, D. USGS (1985). FPFIT, FPPLOT, and FPPAGE: Fortran computer programs for calculating and displaying earthquake fault-plane solutions. *US Geol. Surv. Open-File Rept. 85, 739*.

Satriano, C., Elia, L., Martino, C., Lancieri, M., Zollo, A., & Iannaccone, G. (2011). PRESTo, the earthquake early warning system for southern Italy: Concepts, capabilities and future perspectives. *Soil Dynamics and Earthquake Engineering*, *31*(2), 137-153.

Snoke, J. A., Lee, W. H. K., Kanamori, H., Jennings, P. C., & Kisslinger, C. (2003). FOCMEC: Focal mechanism determinations. *International handbook of earthquake and engineering seismology*, *85*, 1629-1630.

Stabile, T. A., Satriano, C., Orefice, A., Festa, G., & Zollo, A. (2012). Anatomy of a microearthquake sequence on an active normal fault. *Scientific reports*, *2*(1), 1-7.

Steinberg, D. M., Rabinowitz, N., Shimshoni, Y., & Mizrachi, D. (1995). Configuring a seismographic network for optimal monitoring of fault lines and multiple sources. *Bulletin of the seismological society of America*, *85*(6), 1847-1857.

Sokos, E., & Zahradník, J. (2013). Evaluating centroid-moment-tensor uncertainty in the new version of ISOLA software. *Seismological Research Letters*, *84*(4), 656-665.

Tape, W., & Tape, C. (2012). A geometric setting for moment tensors. *Geophysical Journal International*, *190*(1), 476-498.

Tarantino, S., Colombelli, S., Emolo, A., & Zollo, A. (2019). Quick determination of the earthquake focal mechanism from the azimuthal variation of the initial P-wave amplitude. *Seismological Research Letters*, *90*(4), 1642-1649.

Trnkoczy, A., Bormann, P., Hanka, W., Holcomb, L. G., & Nigbor, R. L. (2009). Site selection, preparation and installation of seismic stations. In *New Manual of Seismological Observatory Practice (NMSOP)* (pp. 1-108). Deutsches GeoForschungsZentrum GFZ.

Vavrycuk, V., P. Adamova, J. Doubravová, and H. Jakoubková (2017). Moment Tensor Inversion Based on the Principal Component Analysis of Waveforms: Method and Application to Microearthquakes in West Bohemia, Czech Republic. Seismological Research Letters 88, 1303–1315, doi 10.1785/0220170027

Weber, E., Iannaccone, G., Zollo, A., Bobbio, A., Cantore, L., Corciulo, M., ... & Satriano, C. (2007). Development and testing of an advanced monitoring infrastructure (ISNet) for seismic early-warning applications in the Campania region of southern Italy. In *Earthquake early warning systems* (pp. 325-341). Springer, Berlin, Heidelberg.

Zollo, A., & Bernard, P. (1991). Fault mechanisms from near-source data: joint inversion of S polarizations and P polarities. *Geophysical Journal International*, *104*(3), 441-451.

639

640 TABLES

641

642

Depth 5 km	Max Distance (km)	No. P-polarities
M_L 1.0 -1.5	30	1
M_L 1.5 - 2.0	49	1
M_L 2.0 - 2.5	57	4
Depth 10 km	**Max Distance (km)**	**No. P-polarities**
M_L 1.0 -1.5	33	1
M_L 1.5 - 2.0	40	5
M_L 2.0 - 2.5	66	6

Table 1 Maximum distance of the farthest triggered seismic station and number of P-wave polarities as function of earthquake magnitude and depth. The values, empirically derived from the ISNet bulletin, are used for the earthquake simulations.

Figure No.	Map	Focal Mechanism Solution	Magnitude Bin	Depth	Noise Level	Dataset
4	Kagan angle misfit	FM1, FM2, FM3	M3	10 km	5%	D1
5	Kagan angle misfit	FM1	M1, M2, M3	10 km	5%	D2, D3
6	focal mechanism parameter misfit	FM1	M1, M2, M3	10 km	5%	D3
7	Kagan angle average	FM1	M1, M2, M3	10 km	5%	D2, D3
8	Kagan angle standard deviation	FM1	M1, M2, M3	10 km	5%	D2, D3
9	focal mechanism error	FM1	M1, M2, M3	10 km	5%	D3
10	Kagan angle misfit	FM1, FM2, FM3	M1, M2, M3	10 km	5%	D3
11	focal mechanism parameter misfit	FM1	M1, M2, M3	5 km	5%	D3
12	Kagan angle misfit	FM1	M1, M2, M3	10 km	30%	D3

Table 2. Summary of the Figures 4-12 with parameters used for earthquake simulations whose results are represented as a specific map.

P-plunge (°)	P-trend (°)	T-plunge (°)	T-trend (°)	Strike (°)	Dip (°)	Rake (°)	Quality
55	344	31	196	325	20	-40	A
51	334	36	181	320	15	-30	A
55	14	31	226	355	20	-40	A
53	205	34	49	180	15	-40	A
55	72	33	272	35	15	-50	A
51	177	32	37	290	80	-110	A
54	292	34	91	10	80	-80	A
77	146	9	7	270	55	-100	B
80	235	10	55	325	55	-90	B
76	103	2	6	110	45	-70	B
76	117	2	214	290	45	-110	B
76	82	7	199	275	40	-110	B
75	190	15	10	280	60	-90	B
75	205	15	25	295	60	-90	B
85	230	5	50	140	40	-90	B
83	146	0	53	150	45	-80	B
80	240	10	60	330	55	-90	B
81	233	5	353	270	50	-80	B
81	347	5	227	130	50	-100	B
55	93	10	198	255	45	-140	C
55	133	10	238	295	45	-140	C
48	130	2	38	275	60	-140	C
48	305	2	37	340	60	-40	C
55	202	7	102	345	60	-130	C
58	121	2	27	270	55	-130	C
58	131	2	37	280	55	-130	C
55	342	7	242	125	60	-130	C
47	138	11	36	165	50	-30	C
49	182	14	289	340	45	-150	C
58	151	2	57	300	55	-130	C
49	168	14	61	190	45	-30	C
59	308	15	64	355	65	-60	C
57	306	14	59	115	40	-140	C
57	76	14	189	245	40	-140	C
45	85	6	348	225	65	-140	C
55	22	7	282	165	60	-130	C
57	241	14	354	50	40	-140	C
55	98	7	198	135	60	-50	C
51	115	2	22	145	55	-40	C
55	147	7	47	290	60	-130	C

715

716 **Table 3.** Fault plane solutions of instrumental seismicity occurred in Irpinia region in 2005-2008 and
717 calculated by De Matteis et al., (2012). The solutions are classified according to a quality code based
718 on the resolution of fault plane kinematics as derived in this study. The result of our simulations
719 suggests a quality as follows: FM1=C, FM2=B, FM3=A.

720
721

FIGURES

727
728
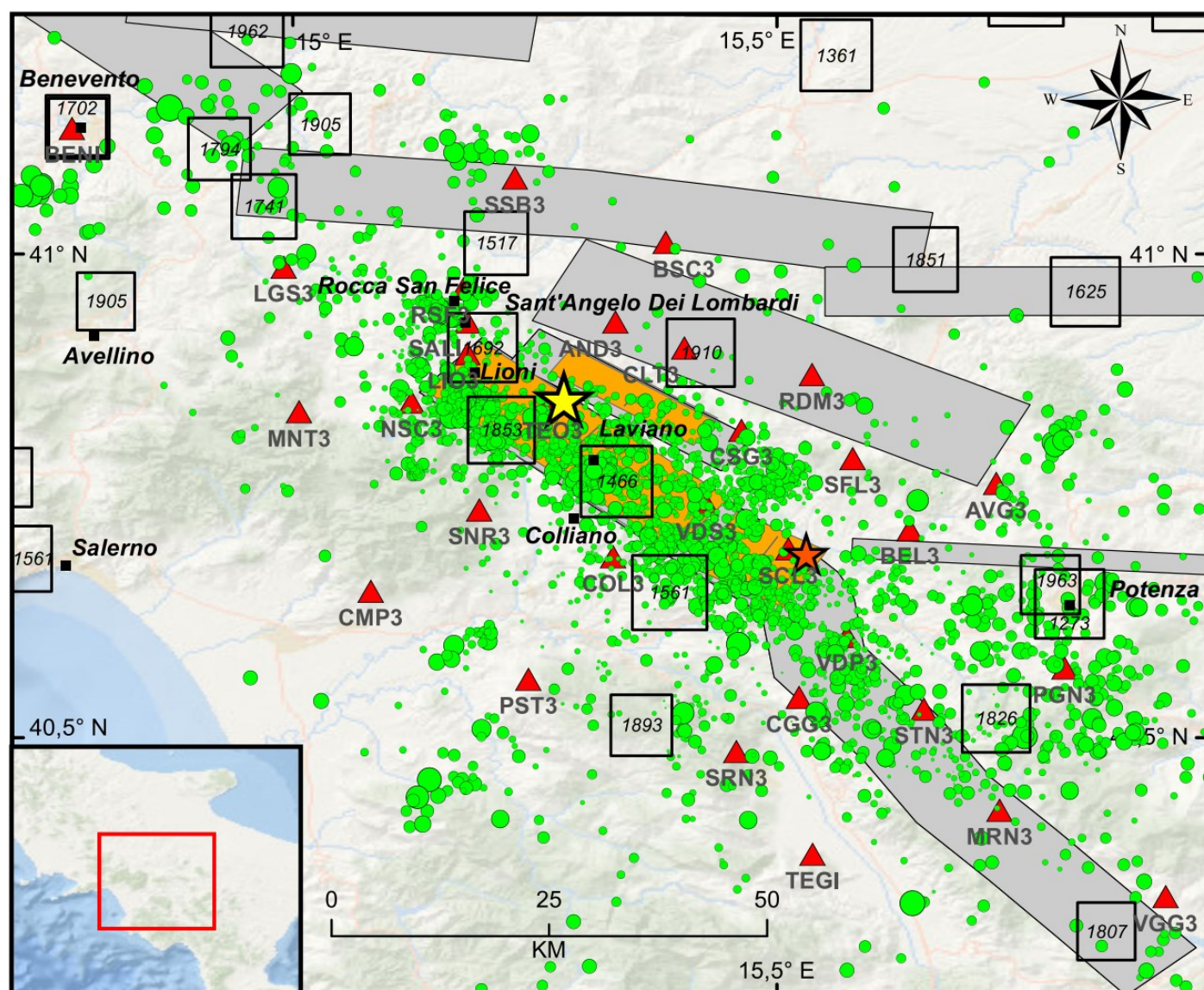
Figure 1. Epicentral map of the earthquakes (green circles) recorded by Irpinia Seismic Network (ISNet, red triangles) from 2008 to 2020 (http://isnet-bulletin.fisica.unina.it/cgi-bin/isnet-events/isnet.cgi). The yellow and orange stars refer to the epicentral location of the 1980, M 6.9, and of the 1996, M 4.9 earthquakes, respectively. Historical seismicity is shown with black squares (I0 ≥ 6–7 MCS). Seismogenic sources related to the Irpinia fault system are indicated by orange rectangles; potential sources for earthquakes larger than M 5.5 in surrounding areas are indicated in grey (Database of Individual Seismogenic Sources, DISS, Version 3.2.1)

736
737
738
739
740
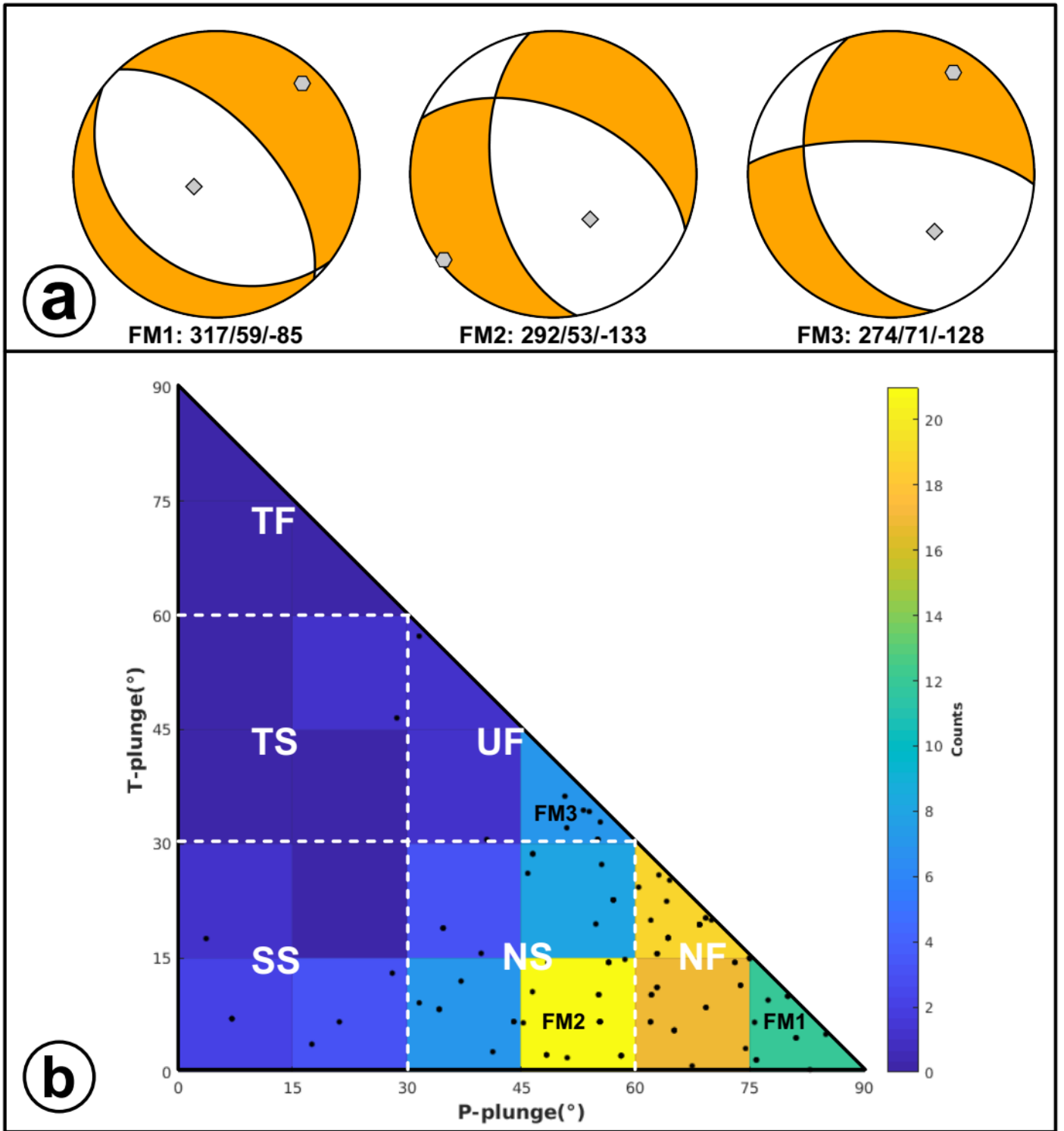
Figure 2. Fault plane solutions used for earthquake simulations. a) From left to right: 1) Ms 6.9, 23rd November 1980 (FM1; Westaway) 2) and 3) Median focal mechanism found from solutions of the 1st (FM2) and 5th (FM3) most populated bin of histogram of panel b. b) Fault plane solutions (black dots) are classified according to the plunge of P- and T-axes with the specific tectonic regimes (Legend: NF, normal fault; NS, normal-strike; SS, strike-slip; TF, thrust ; TS, thrust-strike; UF, unknown fault). The number of earthquakes (colour bar) is counted in bins of 15° × 15°.
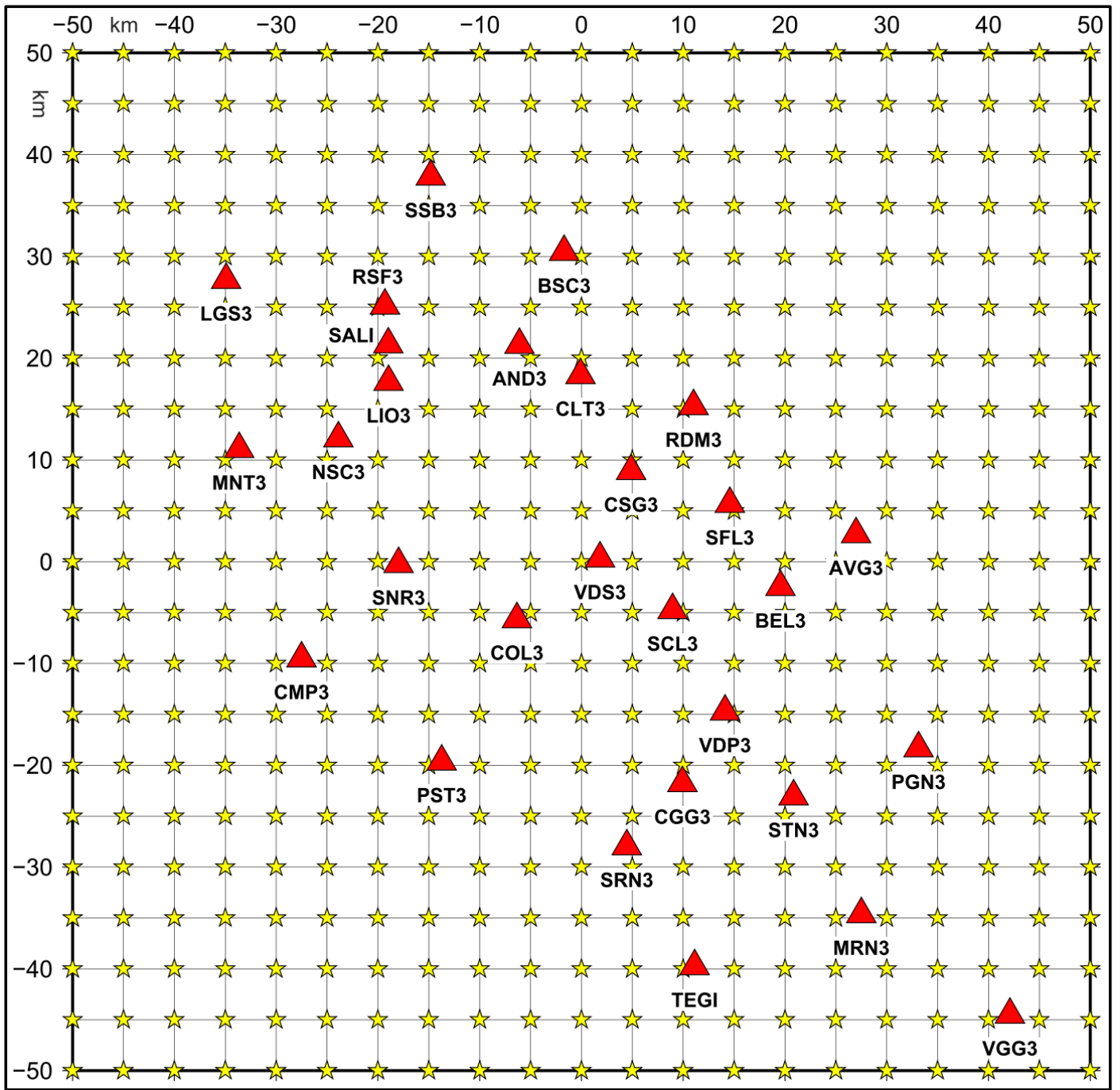
Figure 3. Regular grid of epicentres (yellow stars) used for simulating earthquakes. The area is 100x100 km² with 5 km of spacing along both horizontal coordinates. Irpinia Seismic Network (ISNet) is reported with red triangles.
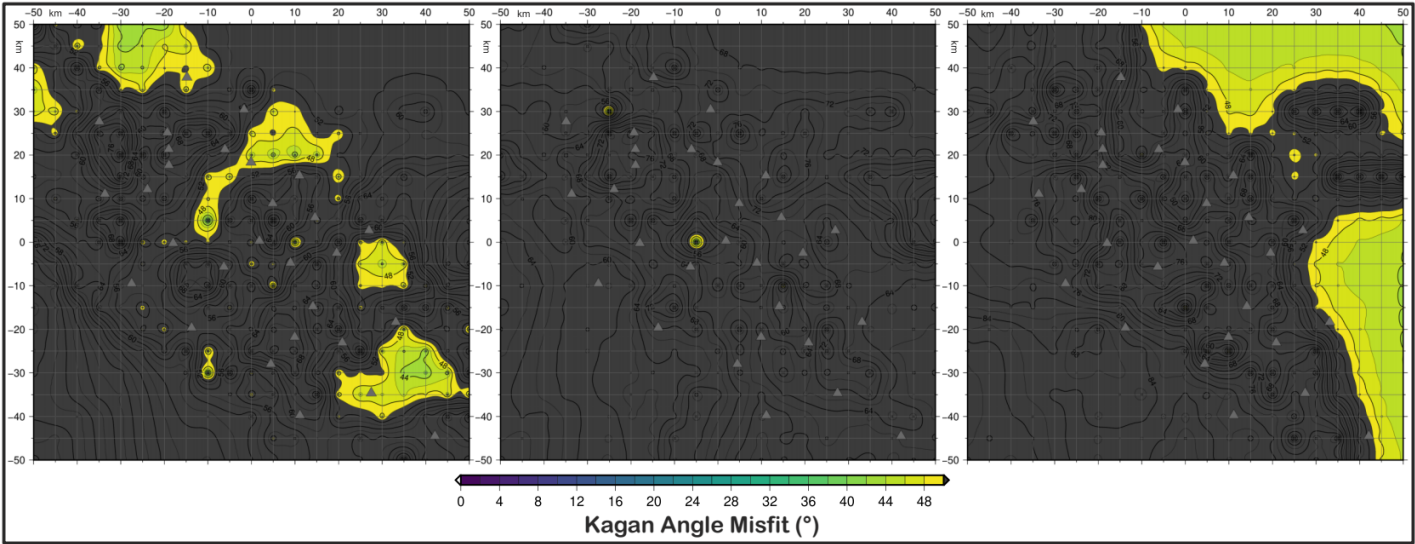
Figure 4. KAM (Kagan angle misfit) map for retrieved focal mechanisms with D1 dataset as input data and simulating earthquakes with M3 magnitude and FM1 (a), FM2 (b) and FM3 (c) theoretical fault plane solution at 10 km depth.
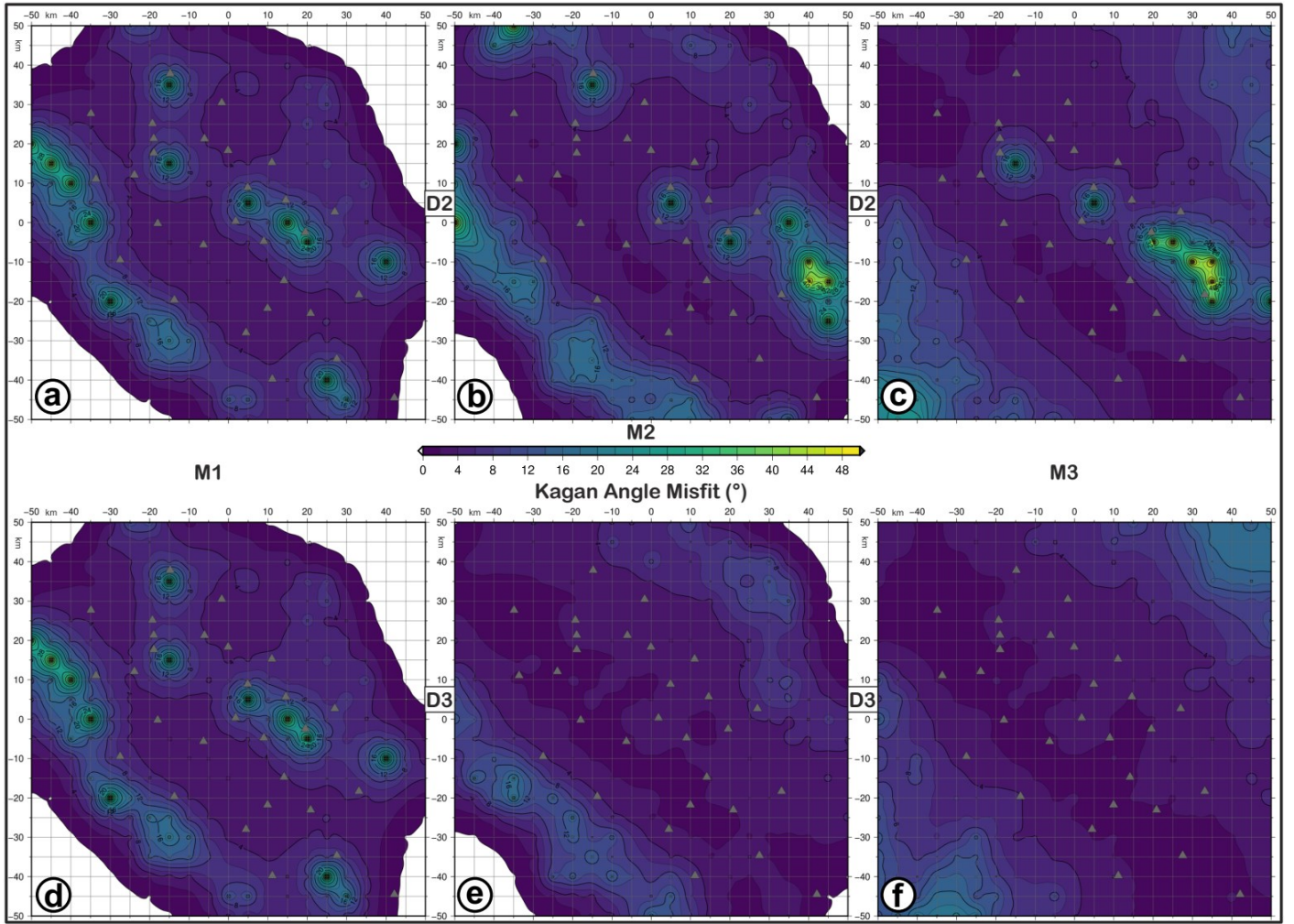
Figure 5. KAM (Kagan angle misfit) map for retrieved focal mechanisms with D2 (a, b, c) and D3 (d, e, f) datasets as input data and simulating earthquakes with M1 (a, d), M2 (b, e) and M3 (c, f) magnitudes and FM1 theoretical fault plane solution at 10 km depth. The level of Gaussian noise is set to 5%.
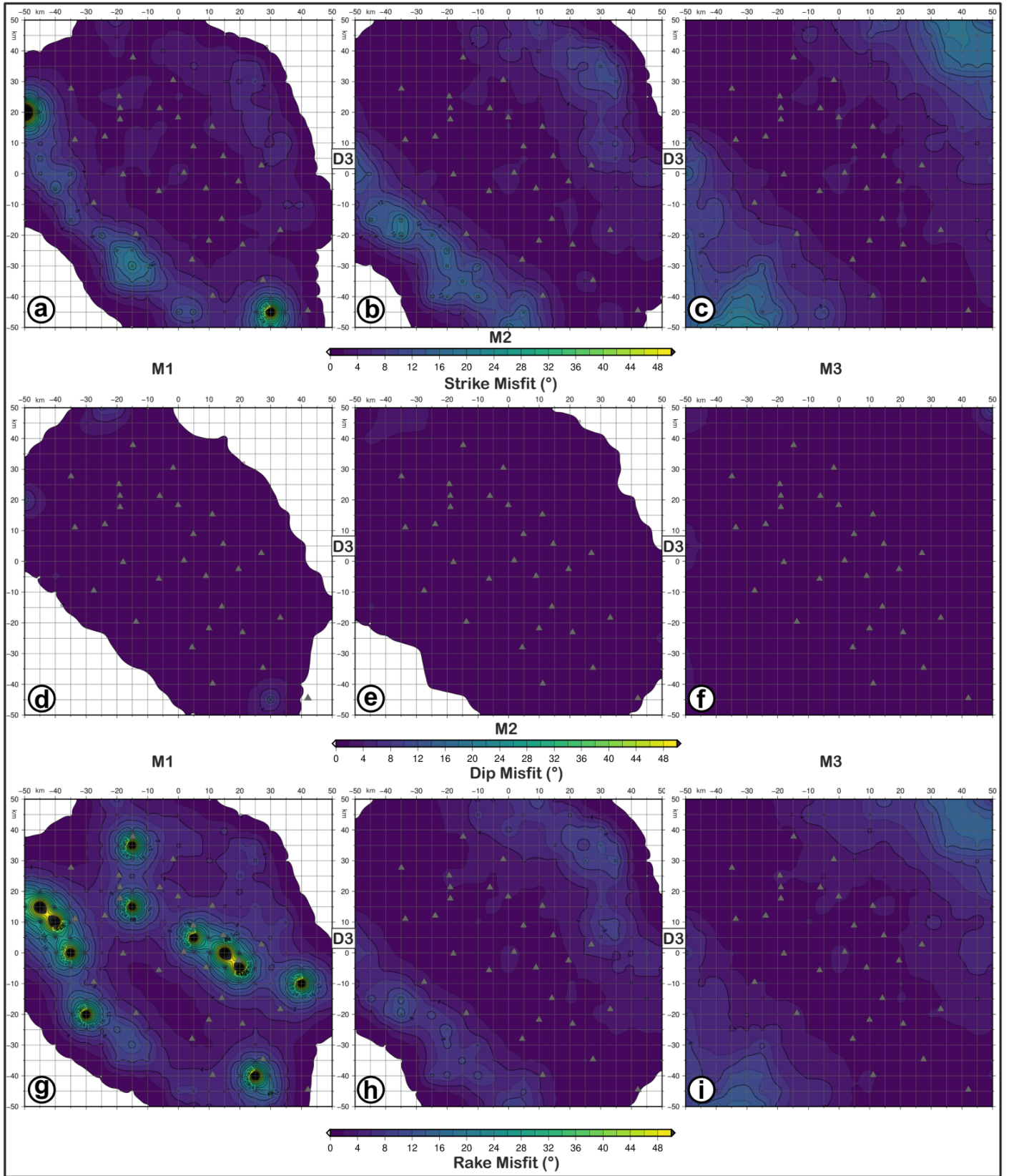
Figure 6. FMM (focal mechanism parameter misfit) maps for retrieved focal mechanisms with D3 datasets as input data and simulating earthquakes with M1 (a, d, g), M2 (b, e, h) and M3 (c, f, i) magnitudes and FM1 theoretical fault plane solution at 10 km depth. a, b, c refer to strike misfit; d, e, f refer to dip misfit; g, h, i refer to rake. The level of Gaussian noise is set to 5%.
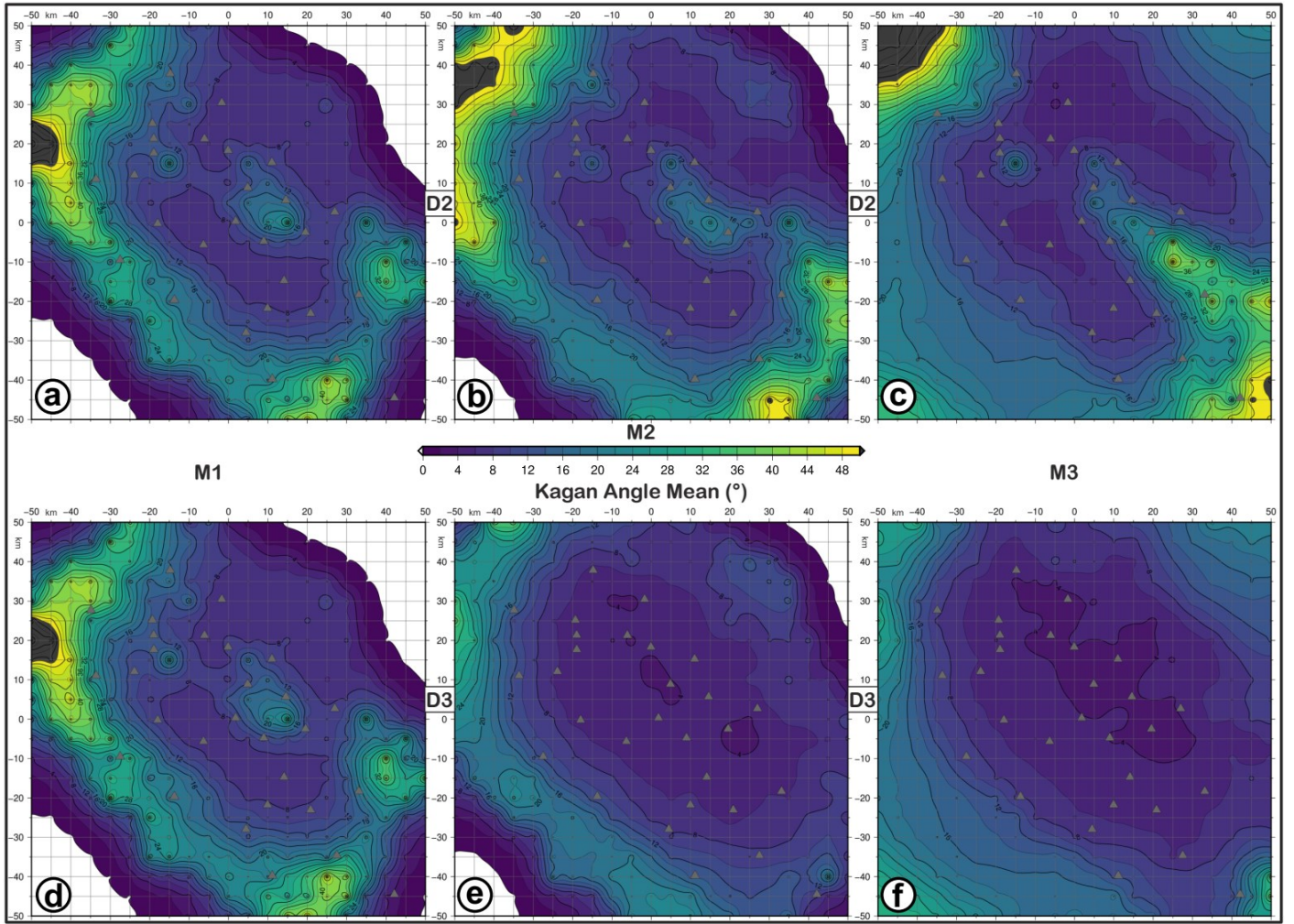
Figure 7. KAA (Kagan angle average) maps for retrieved focal mechanisms with D2 (a, b, c) and D3 (d, e, f) datasets as input data and simulating earthquakes with M1 (a, d), M2 (b, e) and M3 (c, f) magnitudes and FM1 theoretical fault plane solution at 10 km depth. The level of Gaussian noise is set to 5%.
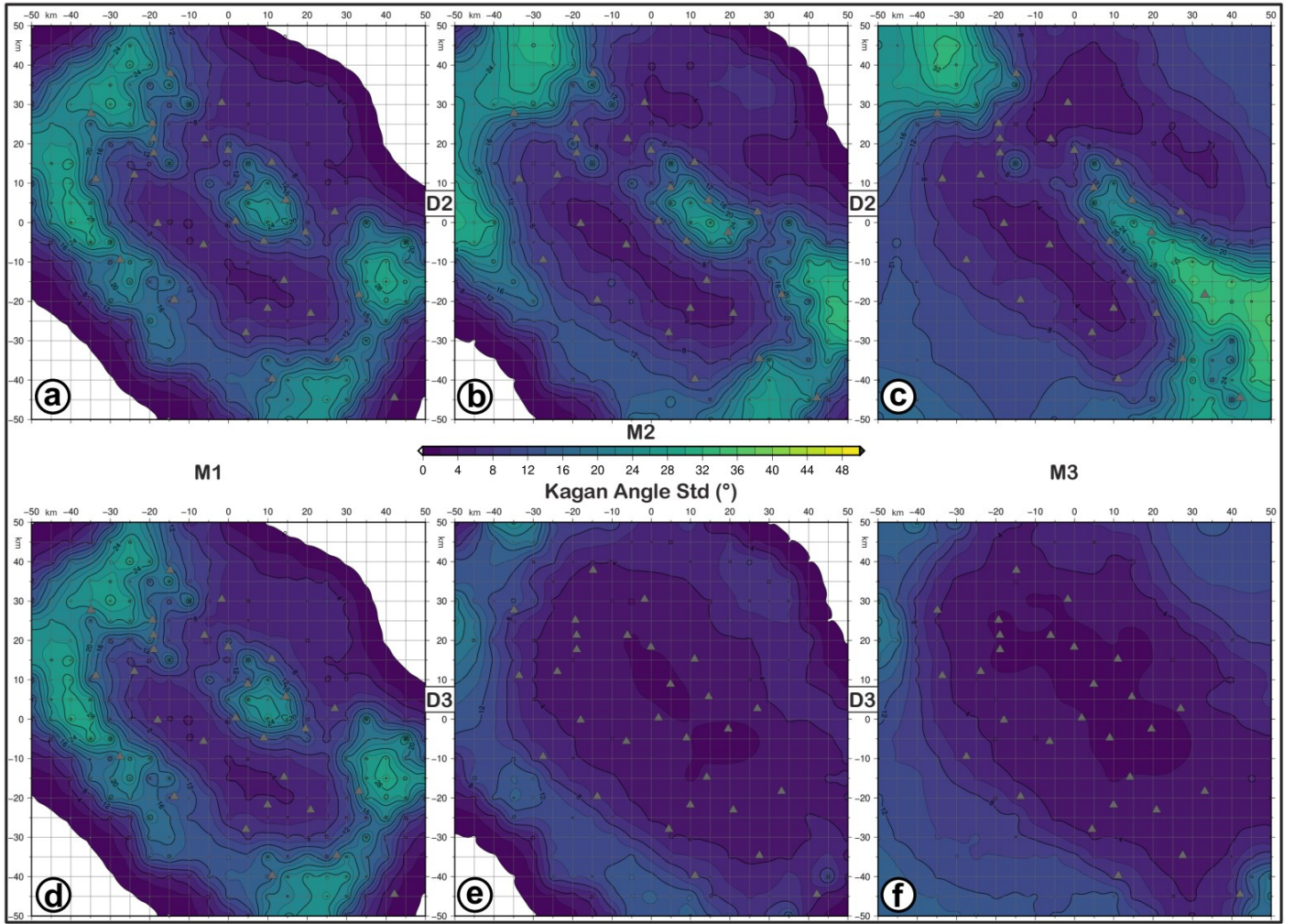
Figure 8. KAS (Kagan angle standard deviation) maps for retrieved focal mechanisms with D2 (a, b, c) and D3 (d, e, f) datasets as input data and simulating earthquakes with M1 (a, d), M2 (b, e) and M3 (c, f) magnitudes and FM1 theoretical fault plane solution at 10 km depth. The level of Gaussian noise is set to 5%.
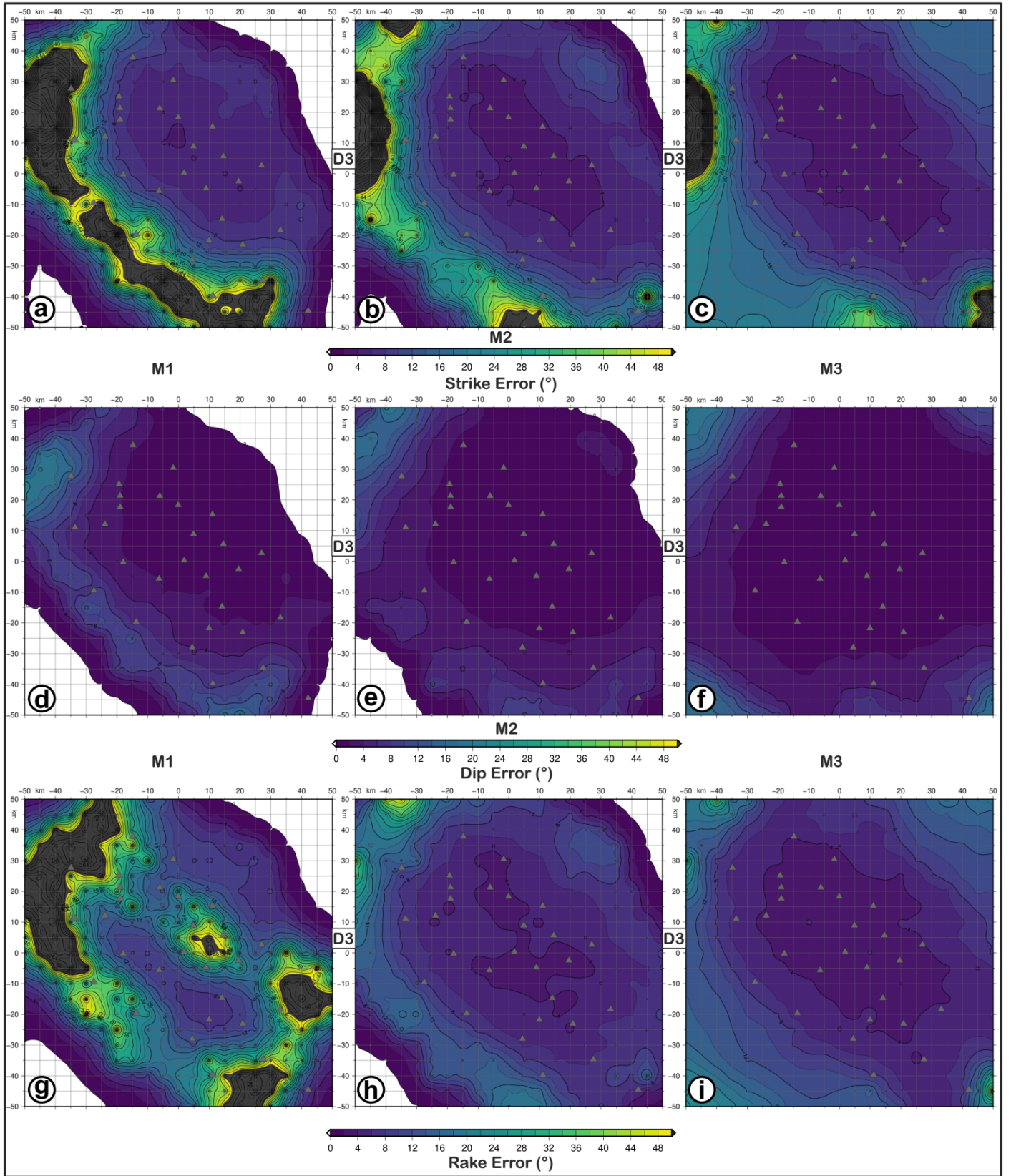
Figure 9. FME (strike, dip and rake error) maps for retrieved focal mechanisms with D3 datasets as input data and simulating earthquakes with M1 (a, d, g), M2 (b, e, h) and M3 (c, f, i) magnitudes and FM1 theoretical fault plane solution at 10 km depth. a, b, c refer to strike error; d, e, f refer to dip error; g, h, i refer to rake error. The level of Gaussian noise is set to 5%.
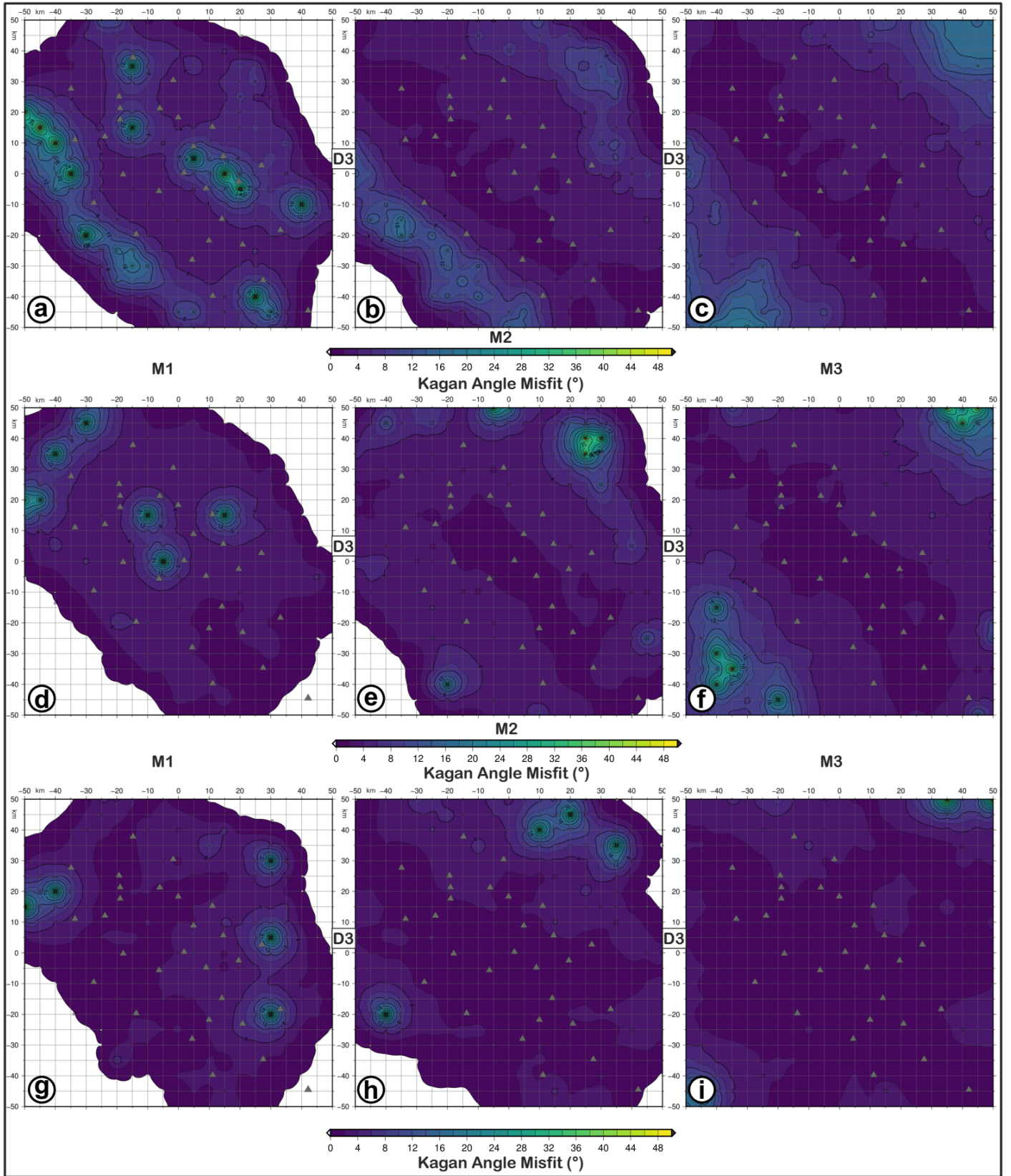
Figure 10. KAM (Kagan angle misfit) maps for retrieved focal mechanisms with D3 datasets as input data and simulating earthquakes with M1 (a, d, g), M2 (b, e, h) and M3 (c, f, i) magnitudes and FM1 (a, b, c), FM2 (d, e, f) and FM3 (g, h, i) theoretical fault plane solution at 10 km depth. The level of Gaussian noise is set to 5%.
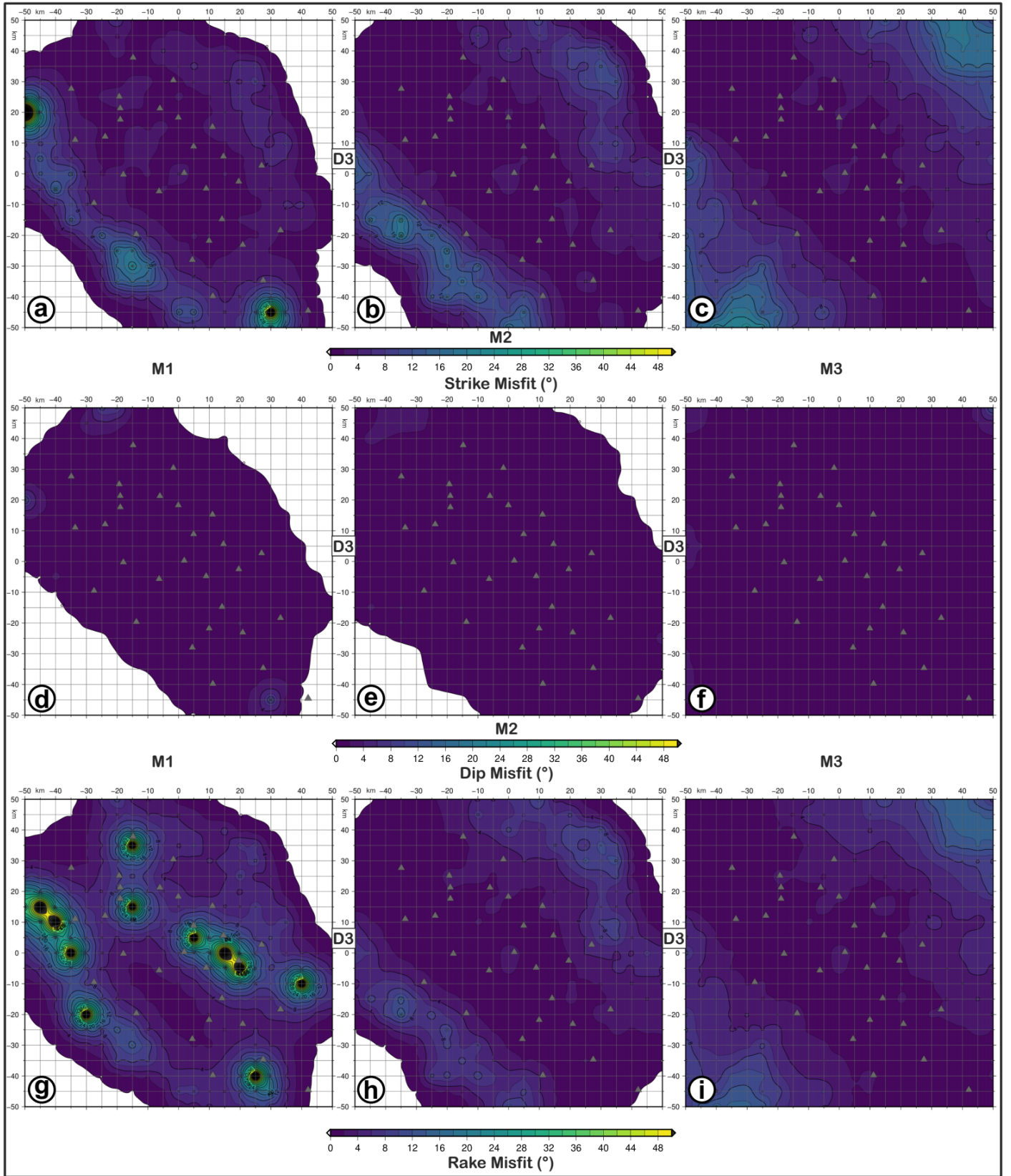
Figure 11. FMM (focal mechanism parameter misfit) maps for retrieved focal mechanisms with D3 datasets as input data and simulating earthquakes with M1 (a, d, g), M2 (b, e, h) and M3 (c, f, i) magnitudes and FM1 theoretical fault plane solution at 5 km depth. a, b, c refer to strike misfit; d, e, f refer to dip misfit; g, h, i refer to rake. The level of Gaussian noise is set to 5%.

869

870
871
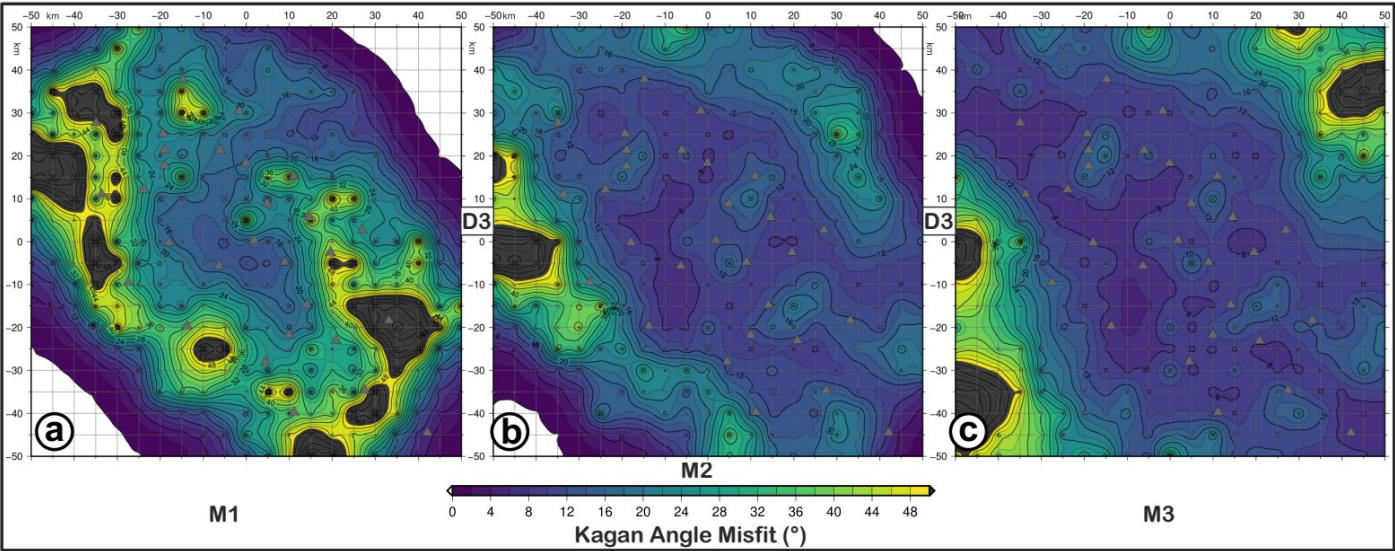
872 **Figure 12.** KAM (Kagan angle misfit) map for retrieved focal mechanisms with D3 (a, b, c) datasets as
873 input data and simulating earthquakes with M1 (a), M2 (b) and M3 (c) magnitudes and FM1 theoretical
874 fault plane solution at 10 km depth. The level of Gaussian noise is set to 30%.
875
876
877
878
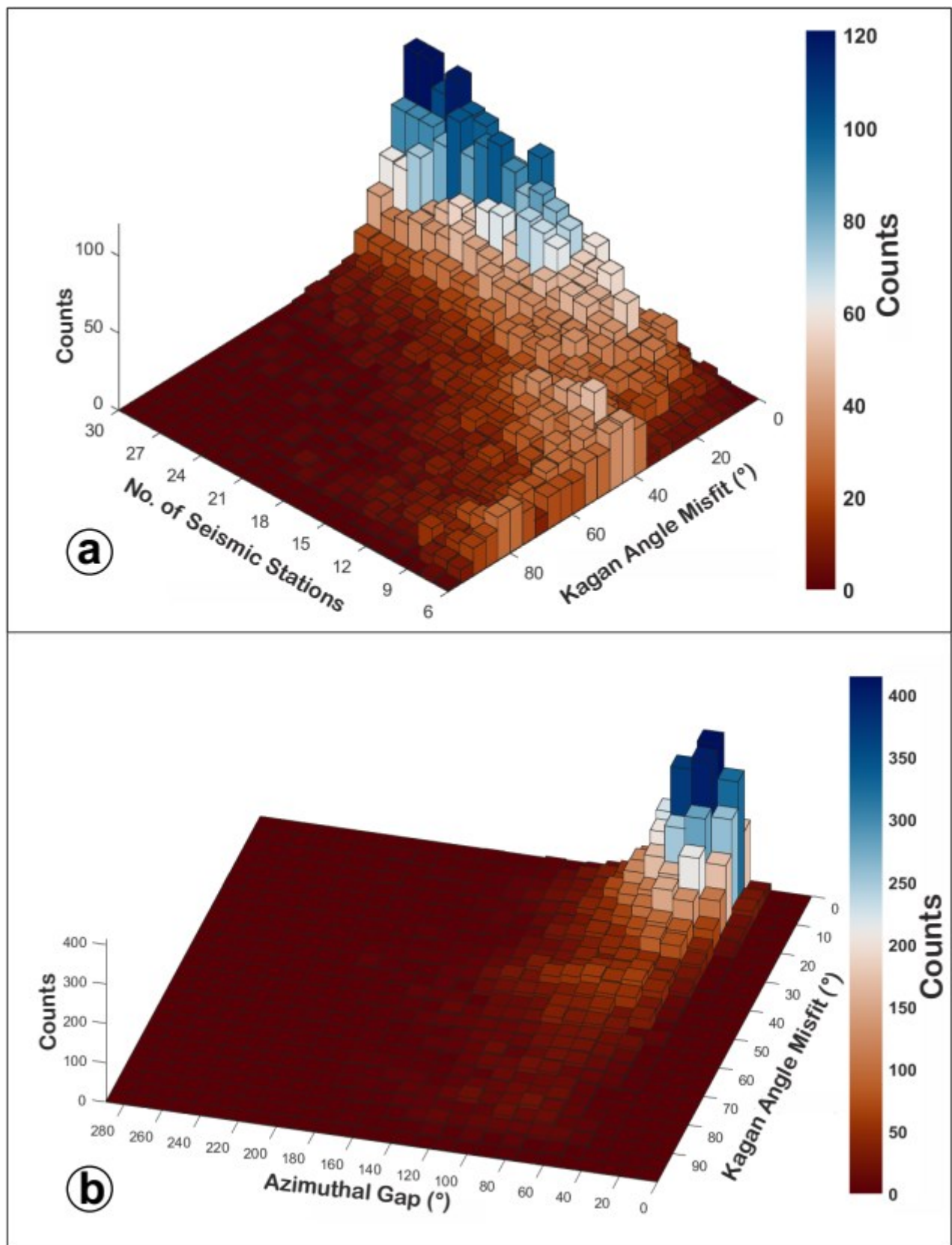
Figure 13. 3D-histograms of the test results in terms of number of stations (a), azimuthal gap (b) and KA misfit. The simulations were carried out with a free network configuration.